Applied Catalysis B: Environmental 221 (2018) 380–392

Contents lists available at ScienceDirect

Applied Catalysis B: Environmental

journal homepage: www.elsevier.com/locate/apcatb

Research Paper

Degradation of atrazine by $Zn_xCu_{1-x}Fe_2O_4$ nanomaterial-catalyzed sulfite under UV–vis light irradiation: Green strategy to generate $SO_4\cdot^-$

Ying Huang[a], Changseok Han[a], Yiqing Liu[a], Mallikarjuna N. Nadagouda[b], Libor Machala[c], Kevin E. O'Shea[d], Virender K. Sharma[e], Dionysios D. Dionysiou[a,*]

[a] Environmental Engineering and Science Program, University of Cincinnati, Cincinnati, OH 45221, USA
[b] Center for Nanoscale Multifunctional Materials, Mechanical & Material Engineering, Wright State University, Dayton, OH 45431, USA
[c] Regional Centre of Advanced Technologies and Materials, Department of Experimental Physics, Faculty of Science, Palacký University, 771 46 Olomouc, Czech Republic
[d] Department of Chemistry and Biochemistry, Florida International University, Miami, FL 33199, USA
[e] Program for the Environmental and Sustainability, Department of Environment and Occupational Health, School of Public Health, Texas A & M University, College Station, TX 77843, USA

ARTICLE INFO

Keywords:
Sulfite
Ferrite
Sulfate radical
Atrazine
UV–vis light

ABSTRACT

Degradation of atrazine, a widely-used herbicide, by a novel advanced oxidation process was investigated through photo-catalyzing sulfite, the precursor of sulfate radical ($SO_4\cdot^-$) in this study, by zinc-copper ferrites ($Zn_xCu_{1-x}Fe_2O_4$) under UV–vis light irradiation. The $Zn_xCu_{1-x}Fe_2O_4$ with different ratios of Zn to Cu was synthesized through a facile sol-gel combustion method, and characterized by X-ray powder diffractometry, scanning electron microscopy, transmission electron microscopy, porosimetry, and UV–vis diffuse reflectance spectroscopy, and by a vibrating sample magnetometer and Mössbauer spectrometer. The $Zn_{0.8}Cu_{0.2}Fe_2O_4$ demonstrated the highest photocatalytic ability to activate sulfite for the degradation of atrazine under current experimental conditions. The sulfate radical generated in the UV–vis light/$Zn_{0.8}Cu_{0.2}Fe_2O_4$/sulfite system was identified as the main reactive species through radical quenching experiments and measuring two important byproducts (atrazine-desethyl and atrazine-desisopropyl). The XPS spectra of fresh and used catalysts were analyzed to further elucidate the reaction mechanisms. There are two possible approaches to produce $SO_4\cdot^-$: the oxidation of sulfite by photo-generated holes and the accelerated decomposition of metal-sulfito complexes (Fe (III)-sulfito and Cu(II)-sulfito) on the surface of $Zn_{0.8}Cu_{0.2}Fe_2O_4$. Based on the detected byproducts, the transformation pathways of atrazine by UV–vis light/$Zn_{0.8}Cu_{0.2}Fe_2O_4$/sulfite were proposed as well. After the complete decomposition of atrazine, the used catalysts could be magnetically recovered using a magnet and no sulfite remained in the system. The results suggest that the UV–vis light/$Zn_{0.8}Cu_{0.2}Fe_2O_4$/sulfite system is a "green" advanced oxidation technology for future application in wastewater treatment.

1. Introduction

Sulfate radical ($SO_4\cdot^-$) based advanced oxidation processes (AOPs) are gaining increasing attention [1,2] because $SO_4\cdot^-$ has a high oxidation potential (2.5-3.1 V) and can react with various recalcitrant organic contaminants [3,4]. $SO_4\cdot^-$ is usually produced from the activation of peroxymonosulfate (PMS) or peroxydisulfate (PDS) by UV [3,5,6], heat [5], ultrasound [7], electro-chemical methods [8], and transition metals [9]. However, after complete decomposition of substrate contaminants, the treated solutions still contain a large fraction of PMS or PDS [4,10], which may cause secondary pollution. Therefore, sulfite is considered as a substitutive precursor for the generation of $SO_4\cdot^-$ in AOPs and it can be simultaneously decomposed along with the organic contaminants [1].

In general, to produce $SO_4\cdot^-$, sulfite is activated homogeneously by transition metals, as shown in Eqs. (1) – (5) [11–13]. Nonetheless, homogeneous activation of sulfite has similar drawbacks to the Fenton reaction, such as: (1) narrow reaction pH ranges due to the hydrolysis of transition metal ions, and (2) precipitation of the formed iron-hydroxyl complexes, which may cause other issues to the follow up treatment processes. To overcome these drawbacks, firstly, photo irradiation is utilized to promote the efficiency of homogeneous activation of sulfite at a wider range of pH, including UV [14], UV–vis light [15] and sunlight [15]. Photo-irradiation accelerates the rate of the decomposition of the metal-sulfito complexes in Eq. (1), which is the rate-limiting step [16,17]. Also, sulfite can be catalyzed heterogeneously to avoid

* Corresponding author.
E-mail address: dionysios.d.dionysiou@uc.edu (D.D. Dionysiou).

http://dx.doi.org/10.1016/j.apcatb.2017.09.001
Received 11 June 2017; Received in revised form 15 August 2017; Accepted 1 September 2017
Available online 09 September 2017
0926-3373/

precipitation. For example, sulfite was activated by $CoFe_2O_4$ to remove metoprolol effectively, whereas the optimum reaction pH was up to 10 [2]. Consequently, a novel photocatalysis technology is needed for the activation of sulfite to generate $SO_4^{\cdot -}$ effectively at the neutral pH condition without any precipitation of metal-hydroxyl species in wastewater treatment applications.

$$xSO_3^{2-} + M^{n+} \rightarrow M(SO_3)_x^{n-2x} \rightarrow xSO_3^{\cdot -} + M^{(n-1)+} (M = Fe, Cu, Co, Mn, etc.) \quad (1)$$

$$SO_3^{\cdot -} + O_2 \rightarrow SO_5^{\cdot -} \quad (2)$$

$$SO_5^{\cdot -} + SO_5^{\cdot -} \rightarrow 2SO_4^{\cdot -} + O_2 \quad (3)$$

$$SO_5^{\cdot -} + SO_3^{2-} \rightarrow SO_4^{2-} + SO_4^{\cdot -} \quad (4)$$

$$SO_5^{\cdot -} + HSO_3^- \rightarrow H^+ + SO_4^{2-} + SO_4^{\cdot -} \quad (5)$$

Zinc ferrite ($ZnFe_2O_4$) is a promising photocatalyst for the activation of sulfite because of its narrow band gap and high photochemical stability. $ZnFe_2O_4$ was used to photo-catalyze oxidants (i.e., hydrogen peroxide (H_2O_2) [18,19], PMS [20] and PDS [10]) and reductants (i.e., oxalic acid [21]) for the effective decomposition of organic dyes under visible light irradiation. Nevertheless, $ZnFe_2O_4$ is not an environmentally friendly material due to its difficulty to recycle. The weak magnetic property of $ZnFe_2O_4$ makes it hard to be removed from the reaction solution by an external magnetic field; however, it can be improved by doping another transition metal into $ZnFe_2O_4$, such as copper [22]. It is also worth mentioning that Cu(II) and Fe(III) have a positive synergistic effect on the homogeneous activation of sulfite [23], providing potential solutions for the heterogeneous catalysis of sulfite. Thus, zinc-copper ferrite nanocomposites ($Zn_xCu_{1-x}Fe_2O_4$) will be used as the photocatalyst to activate sulfite, and such a process as reported herein has not yet been studied.

Our goal in this study is twofold. Firstly, it is important to find out whether the UV–vis light/$Zn_xCu_{1-x}Fe_2O_4$/sulfite technology is both efficient and environmentally friendly to remove organic contaminants. Specifically, $Zn_xCu_{1-x}Fe_2O_4$ was synthesized via a sol-gel combustion method and used to catalyze sulfite under UV–vis light irradiation to degrade atrazine ($C_8H_{14}ClN_5$), which is a widely-used and frequently detected herbicide in wastewater. To the best of our knowledge, it is the first study to apply heterogeneous photocatalysis to activate sulfite in the degradation of organic chemicals. The physical, optical, and magnetic properties of as-synthesized materials were characterized, operation parameters were optimized, and the residual concentration of sulfite after reaction was measured. Secondly, we predicted that the produced $SO_4^{\cdot -}$ mainly contributed to the degradation of atrazine. Therefore, possible mechanisms for the activation of sulfite by $Zn_xCu_{1-x}Fe_2O_4$/UV-vis light and potential degradation pathways of atrazine were proposed based on XPS analysis, quenching experiments, and detected reaction byproducts. This study provides a fundamental understanding and theoretical support for the applications of UV-vis light/$Zn_xCu_{1-x}Fe_2O_4$/sulfite technology in wastewater treatment.

2. Experimental methods

2.1. Preparation of $Zn_xCu_{1-x}Fe_2O_4$ nanoparticles

Magnetic ferrites of $Zn_xCu_{1-x}Fe_2O_4$ (x = 0, 0.2, 0.33, 0.5, 0.67, 0.8, and 1) were synthesized by a sol-gel combustion process with citric acid, as previously reported [24,25]. Typically, zinc nitrate hexahydrate ($Zn(NO_3)_2{\cdot}6H_2O$), copper nitrate hemi(pentahydrate) ($Cu(NO_3)_2{\cdot}2.5H_2O$), and ferric nitrate nonahydrate ($Fe(NO_3)_3{\cdot}9H_2O$) were dissolved in Milli-Q water at a specified stoichiometric ratio, followed by adding citric acid solution (25 mM) dropwise until the molar ratio of citric acid to Fe cations reached 3:2. After adjusting the pH of the resulting mixture with ammonium hydroxide to around 5, it was stirred rigorously at 60 °C towards the formation of a gel-like network, dried in an oven at 90 °C for 6 h, and calcined at 400 °C for 2 h. Finally, the calcined particles were ground, washed with ethanol, 0.1 M H_2SO_4 and Milli-Q water, and dried at 100 °C for 12 h.

2.2. Characterization

The surface morphology of the as-prepared samples was observed with a scanning electron microscope (SEM, FEI SCIOS) and a high-resolution transmission electron microscope (HR-TEM, JEOL JEM-2010). The structure and crystal phase of the as-prepared samples were analyzed using X-ray powder diffraction (XRD, PANalytical). The Brunauer–Emmett–Teller (BET) surface area and optical property of the samples were measured by TriStar 3000 surface area analyzer (Micromeritics) and UV–vis spectrophotometer (Shimadzu 2501 PC) mounted with an integrating sphere accessory (ISR1200), respectively. The transmission ^{57}Fe Mössbauer spectra were collected at room temperature using a Mössbauer spectrometer in a constant acceleration mode with a ^{57}Co(Rh) source. The isomer shift values were related to metallic α-Fe at room temperature. The spectra were evaluated by the software MossWinn 4.0. The magnetic data were measured on powder samples using a Quantum Design physical properties measurement system (PPMS Dynacool system) with the VSM option. The experimental data were corrected for the diamagnetism and signal of the sample holder. The hysteresis loops were recorded at a temperature of 300 K in externally magnetic fields ranging from − 9 to + 9 T. The changes of chemical oxidation states of elements on the surface of fresh and used catalysts were recorded by high-resolution X-ray photoelectron spectroscopy (XPS) employing a PHI 5000 VersaProbe II XPS system (Physical Electronics) using a monochromatic Al-K_α source (15 kV, 50 W) with photon energy of 1486.7 eV. Dual beam charge compensation was used for all the measurements. All spectra were measured in a vacuum of 1.4×10^{-7} Pa and at room temperature of 22 °C. For the high-resolution spectra, pass energy of 23.500 eV and step size of 0.200 eV were used. The XPS patterns were evaluated with the MultiPak (Ulvac-PHI, Inc.) software. All binding energy values were referenced to the C1 s peak at 284.80 eV. The surface charges of as-prepared catalysts in solutions with different pH values were characterized using Zeta potential analyzer (NanoBrook Omni).

2.3. Catalytic degradation experiments

Photocatalytic experiments were conducted using a 500 W Xenon lamp (Newport 67005) for UV–vis light irradiation. The light was filtered by Air Mass 1.5 global filter (Newport Corporation) and FSQ-KG5 heat absorbing glass filter (Newport Corporation), and the filtered light spectrum was in the range of 350–700 nm, as shown in Fig. S1 in Supporting Information.

Unless stated otherwise, degradation experiments were carried out in a 50-mL crystallizing dish, covered with a round quartz cover, and shaken by a basic shaker (IKA KS 130). $Zn_xCu_{1-x}Fe_2O_4$ nanoparticles were firstly dispersed into 20 mL atrazine solution (4.4 μM), and the mixture was shaken for 15 min to achieve the adsorption/desorption equilibrium between the catalyst and the target compound. Then, 0.1 mL of sulfite stock solution (100 mM) was added into the solution followed by adjusting the initial pH to 7.2 with 0.1 M H_2SO_4 as quickly as possible. The sulfite stock solution was always freshly prepared. Once the photo-degradation was initiated, 200 μL samples were taken at given time intervals of 2, 5, 10, 15, 20, and 30 min, immediately quenched by 200 μL methanol (34.7 M), filtered by 0.2 μm PTFE syringeless filter (Whatman, GE Healthcare Life Sciences), and then analyzed by high-performance liquid chromatography (HPLC). All experiments were conducted in triplicate at room temperature.

2.4. Analysis methods

The concentration of atrazine was determined by an Agilent 1100

HPLC equipped with a photodiode array detector. An Eclipse XDB-C_{18} column (5 μm, 4.6 × 150 mm) kept at 25 °C was used as the stationary phase. The mobile phase was pure acetonitrile and Milli-Q water (60:40, v/v) with a flow rate of 0.4 mL min^{-1}. The sample injection volume was 20 μL, and the detection wavelength was 222 nm.

To identify hydroxyl radical (·OH), terephthalic acid (TPA) was used as a ·OH dosimeter, and the fluorescence spectra of formed 2-hydroxyterephthalic acid (TPA-OH) was measured on a Multi-Mode Microplate Reader (FlexStation 3) with an excited wavelength of 315 nm and a detection wavelength of 425 nm. The pH of the sample was adjusted to 9 by NaOH before analysis, because the fluorescence intensity of TPA-OH is constant only in a certain pH range of 6–10 [26].

Two specific byproducts, atrazine-desethyl (DEA) and atrazine-desisopropyl (DIA), were measured by a Triple Quad liquid chromatography/mass spectrometer (QQQ-LC/MS). The transformation products were detected using a quadrupole time-of-flight liquid chromatography/mass spectrometer (Q-TOF-LC/MS, Agilent G6540A). Both instruments were operated in a positive mode with a scan range of *m/z* 100–350. A C_{18} Discovery HS (Supelco) column (5 μm particle size, 150 × 2.1 mm) was applied as a separation column. The mobile phase, consisting of A (H_2O + 0.1% HCOOH) and B (CH_3CN + 0.1% HCOOH), was linearly increased from 5% B to 85% in 6 min, kept for 2 min, and back to 5% B in the last 2 min at a flow rate of 0.5 mL min^{-1}. The sample injection volume was 20 μL.

A colorimetric procedure with 5,5′-Dithiobis-2-nitrobenzoic acid (DTNB) was utilized to determine the concentration of sulfite by spectrometry [1]. In brief, 1 mL filtered sample (by 0.1 μm Magna™ nylon membrane filter) was added into a mixture of 1 mL ethylenediaminetetraacetic acid disodium salt (EDTA-Na_2, 1 mM), 2 mL DTNB (1 mM), and 7 mL Na_2HPO_4/NaH_2PO_4 buffer solution (10 mM, pH = 7). The obtained solution was mixed well, kept for 3 min, and then measured by a UV–vis light spectrophotometer (Agilent 8543). The quantification of dissolved zinc, ferric and copper cations was performed by an atomic absorption spectroscope (AAnalyst 300).

3. Results and discussion

3.1. Characterization of $Zn_xCu_{1-x}Fe_2O_4$

The prepared $Zn_xCu_{1-x}Fe_2O_4$ samples (x = 0, 0.2, 0.33, 0.5, 0.67, 0.8, and 1) were characterized by XRD, as shown in Fig. 1a. In each case, all the diffraction peaks can be readily indexed to the spinel copper zinc ferrite ($Cu_{0.5}Zn_{0.5}Fe_2O_4$, PDF # 01-077-0012). No other phases were detected in the XRD patterns, confirming good crystallinity of the $Zn_xCu_{1-x}Fe_2O_4$ samples.

In addition, the morphology and microstructure of $Zn_{0.8}Cu_{0.2}Fe_2O_4$ were further characterized by SEM, TEM and HR-TEM. The SEM image in Fig. 1b showed that the sol-gel combustion method leads to agglomerated nanoparticles. An enlarged TEM image (Fig. 1c) showed a primary particle size of approximately 27 nm. A typical HR-TEM image (Fig. 1d) showed an interplanar distance of 0.257 nm corresponding to the (311) spinel plane of ferrites, which confirmed the formation of an individual ferrite nanocrystal.

The specific compositions of $ZnFe_2O_4$, $Zn_{0.8}Cu_{0.2}Fe_2O_4$ and $CuFe_2O_4$ were identified by the Mössbauer spectrum at room temperature. The Mössbauer spectra of $ZnFe_2O_4$ (Fig. 2a) and $Zn_{0.8}Cu_{0.2}Fe_2O_4$ (Fig. 2b) showed by similar patterns that the quadrupole splitting of the sextet is close to zero, which is typical for cubic spinel symmetry of the crystal structure in ferrites [27]. The intensity of the doublet corresponding to superparamagnetic ferrite nanoparticles in the spectrum of $ZnFe_2O_4$ is higher than that of $Zn_{0.8}Cu_{0.2}Fe_2O_4$, indicating that $ZnFe_2O_4$ has more superparamagnetic fraction. The intensity of magnetic splitting in the spectrum of $Zn_{0.8}Cu_{0.2}Fe_2O_4$ is higher than that of $ZnFe_2O_4$, confirming the more relative content of ferrimagnetic phase in $Zn_{0.8}Cu_{0.2}Fe_2O_4$. The Mössbauer spectrum of $CuFe_2O_4$ sample (Fig. 2c) is presented by two sextets corresponding to $CuFe_2O_4$ (quadrupole splitting close to zero, lower hyperfine magnetic field) and α-Fe_2O_3 (with typical value of quadrupole splitting of $-$ 0.20 mm s^{-1} and lower hyperfine magnetic field). The low intensity of doublet in the spectrum of $CuFe_2O_4$ sample suggested the least fraction of superparamagnetic phase.

The various compositions of $ZnFe_2O_4$, $Zn_{0.8}Cu_{0.2}Fe_2O_4$ and $CuFe_2O_4$ lead to different physical properties including the magnetic property, specific surface area, morphology, microstructure, and optical property. The magnetic property was measured by recording the hysteresis loop of $ZnFe_2O_4$, $Zn_{0.8}Cu_{0.2}Fe_2O_4$, and $CuFe_2O_4$ (Fig. 2d). Interestingly, $Zn_{0.8}Cu_{0.2}Fe_2O_4$ showed the highest saturation magnetization and the lowest coercivity value at room temperature (Table S1 in Support Information), which is correlated to the highest fraction of ferrimagnetic phase in $Zn_{0.8}Cu_{0.2}Fe_2O_4$ and the absence of α-Fe_2O_3 phase, generally reducing the net magnetization of the sample. The highly magnetic property indicated that $Zn_{0.8}Cu_{0.2}Fe_2O_4$ could easily be recollected compared to the other samples by an external magnetic field from the reaction solution (Fig. S2 in Supporting Information).

The specific surface area is of importance for heterogeneous catalysts since it is directly associated with active sites and adsorption capacities of catalysts. The surface areas of $ZnFe_2O_4$, $Zn_{0.8}Cu_{0.2}Fe_2O_4$, and $CuFe_2O_4$ were investigated using nitrogen adsorption-desorption isotherms, as shown in Fig. 2e. The three isotherm curves are of typical type IV pattern with a long and narrow hysteresis loop at relative pressure (P/P_0) from 0.7 to 1.0, indicating the mesoporous structure of the as-prepared samples [28]. The measured BET specific surface area of $ZnFe_2O_4$, $Zn_{0.8}Cu_{0.2}Fe_2O_4$, and $CuFe_2O_4$ are 35.8, 25.9 and

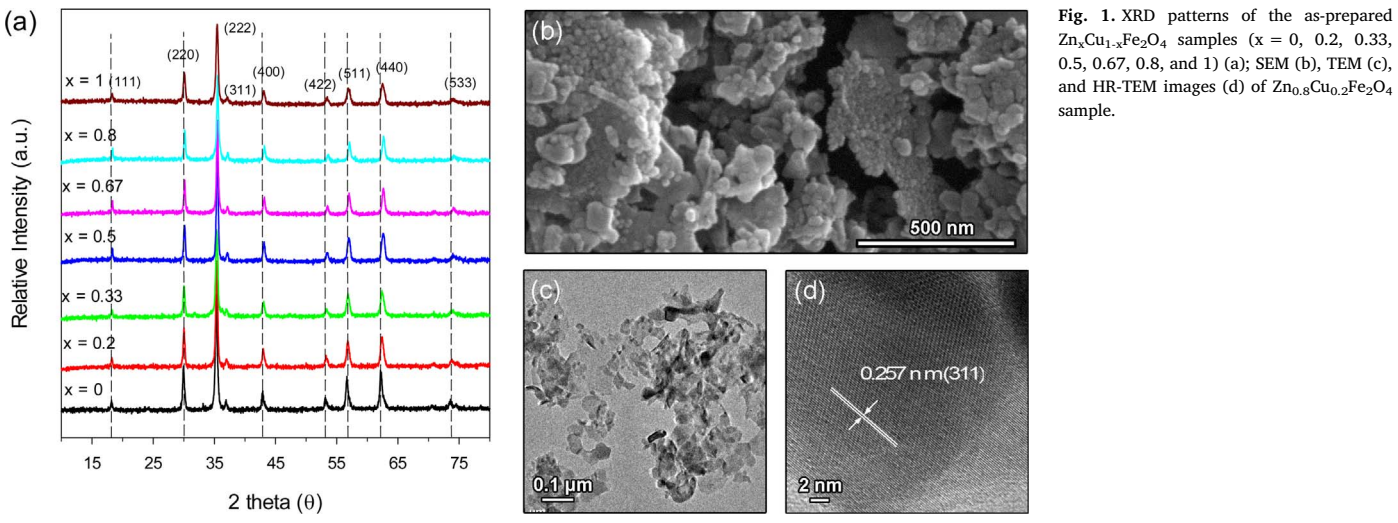

Fig. 1. XRD patterns of the as-prepared $Zn_xCu_{1-x}Fe_2O_4$ samples (x = 0, 0.2, 0.33, 0.5, 0.67, 0.8, and 1) (a); SEM (b), TEM (c), and HR-TEM images (d) of $Zn_{0.8}Cu_{0.2}Fe_2O_4$ sample.

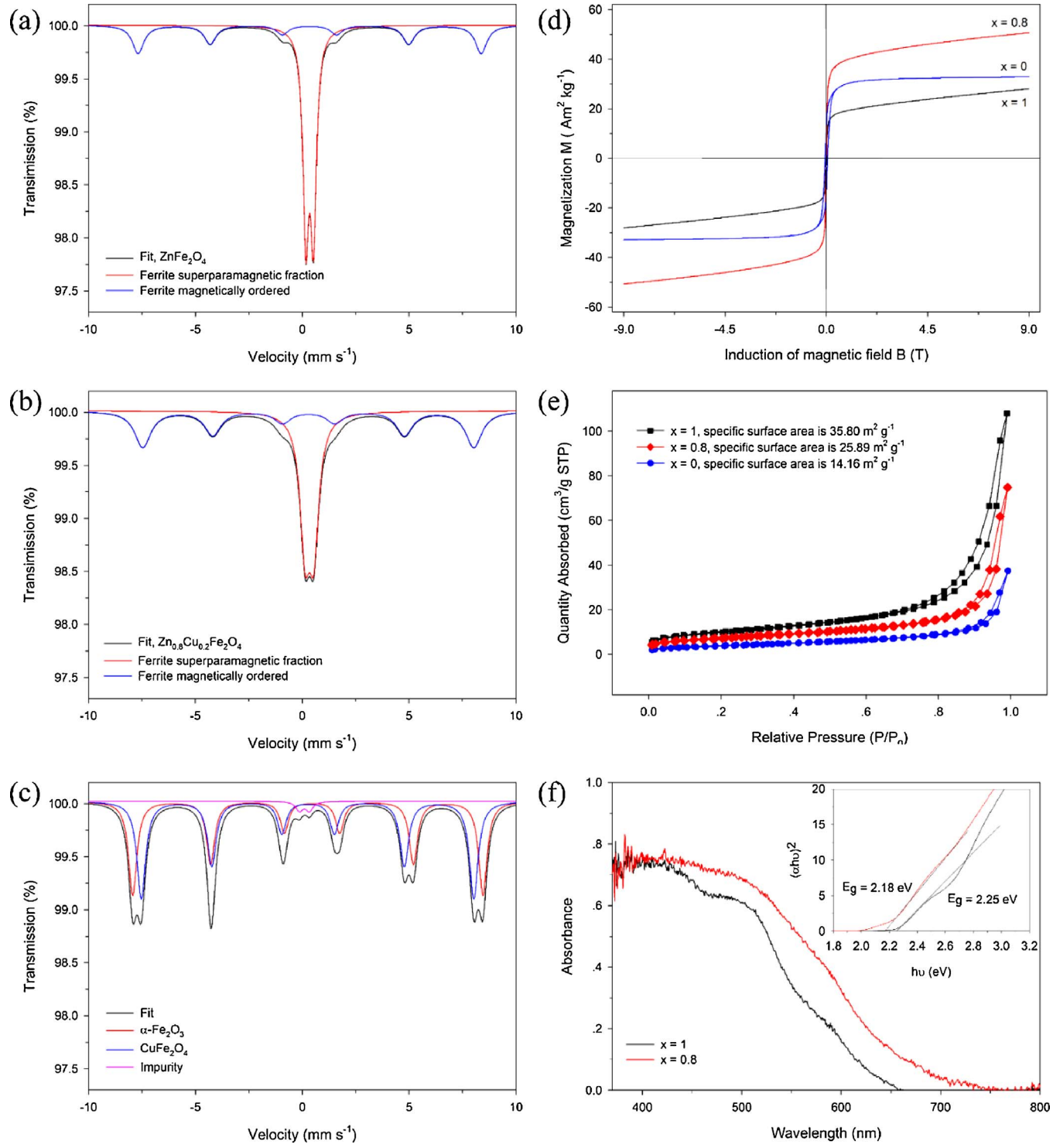

Fig. 2. Room temperature Mössbauer spectrum of $ZnFe_2O_4$ (a), $Zn_{0.8}Cu_{0.2}Fe_2O_4$ (b), and $CuFe_2O_4$ (c); magnetic hysteresis loops (d) and N_2 isotherms (e) of $Zn_xCu_{1-x}Fe_2O_4$ samples (x = 0, 0.8, and 1); and UV–vis light absorption spectra of $Zn_xCu_{1-x}Fe_2O_4$ samples (x = 0.8 and 1) (f).

14.2 $m^2\ g^{-1}$, respectively.

Furthermore, the optical properties of the as-prepared $Zn_{0.8}Cu_{0.2}Fe_2O_4$ and $ZnFe_2O_4$ were characterized through UV–vis light absorption spectra. As shown in Fig. 2f, the estimated band gap of $Zn_{0.8}Cu_{0.2}Fe_2O_4$ can be estimated to be 2.18 eV via Tauc equation, which is a little smaller than that of $ZnFe_2O_4$ (2.25 eV). This result indicated that the $Zn_{0.8}Cu_{0.2}Fe_2O_4$ might be effectively activated under UV–vis light irradiation.

3.2. The catalytic activity and stability of prepared samples

As shown in Fig. 3a, more than 95% of atrazine was degraded in 30 min by $Zn_{0.8}Cu_{0.2}Fe_2O_4$/sulfite under UV–vis light irradiation. Adsorption of atrazine on the catalyst and direct photolysis of atrazine by UV–vis light were negligible at these experimental conditions. Interestingly, atrazine could be slightly degraded when sulfite was introduced in the absence of catalysts and UV–vis light, because atrazine

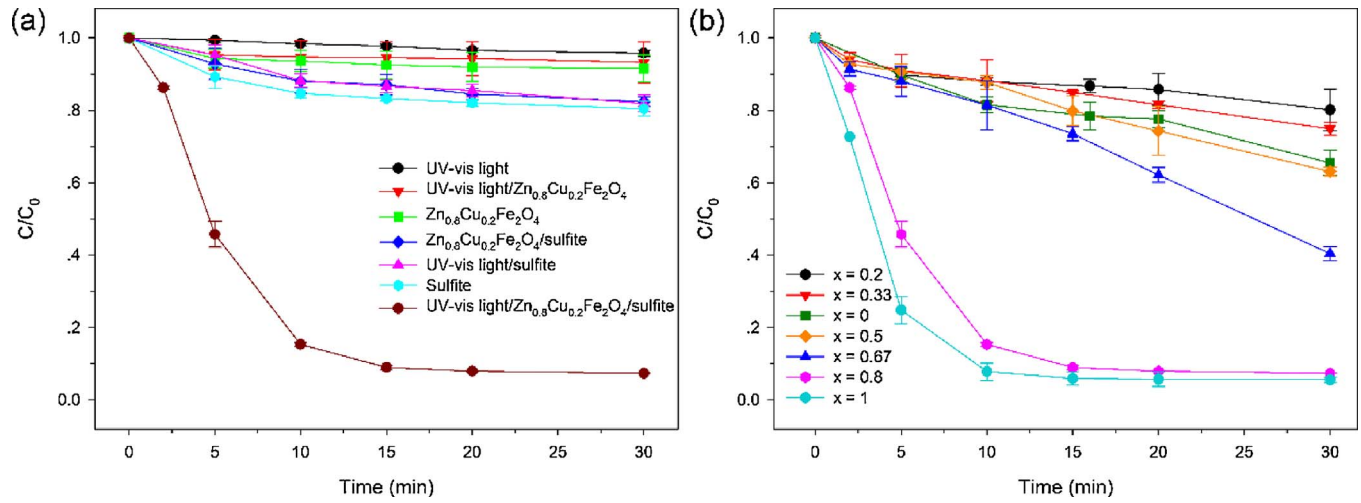

Fig. 3. Atrazine degradation in photocatalytic sulfite oxidations (a), and in catalytic sulfite oxidation by $Zn_xCu_{1-x}Fe_2O_4$ samples (x = 0, 0.2, 0.33, 0.5, 0.67, 0.8, and 1) (b). Conditions: C_0(atrazine) = 4.4 μM, C_0(sulfite) = 0.5 mM, C_0(catalyst) = 200 mg L^{-1}, initial pH = 7.2, V = 20 mL, temperature = 293 K.

as an N-chloric compound can be directly reduced by sulfite [29,30]. Compared to the heterogeneous process, the degradation of atrazine through homogeneous catalytic oxidation of sulfite by leached metal ions was negligible, as shown in Fig. S3 in Supporting Information.

In addition, the effect of different ratios of Zn to Cu in zinc-copper ferrites on atrazine degradation was investigated (Fig. 3b). When the dosage of different catalysts was fixed, the degradation was proportional to an increase of Zn: Cu in the range of 0.2 − 1. This phenomenon might be attributed to the formation of hematite, caused by the introduction of Cu into zinc ferrite, which has hardly any catalytic ability for sulfite [2]. $ZnFe_2O_4$ showed the highest photocatalytic ability for sulfite and had the largest amount of superparamagnetic fraction, indicating that the superparamagnetic fraction in ferrite seems to play a significant role in the activation of sulfite. However, $Zn_{0.8}Cu_{0.2}Fe_2O_4$ held both a strong magnetic property and a high amount of superparamagnetic fraction, and thus it might be a better choice for the activation of sulfite due to its magnetically removable and photocatalytic capacity.

The chemical stability and reusability of prepared $Zn_{0.8}Cu_{0.2}Fe_2O_4$ were tested for its application in wastewater treatment. As shown in Fig. 4, $Zn_{0.8}Cu_{0.2}Fe_2O_4$ still retained good catalytic activity after the fifth repeat, indicating its high stability in the reaction system. The

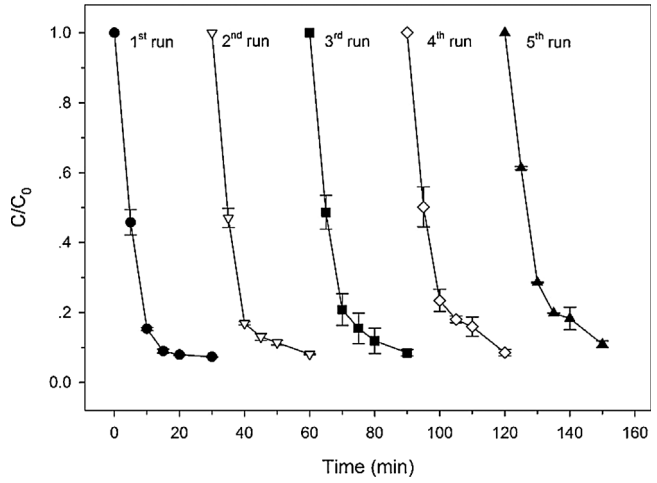

Fig. 4. Atrazine degradation in five continuous batch runs by UV–vis light/$Zn_{0.8}Cu_{0.2}Fe_2O_4$/sulfite. Conditions: C_0(atrazine) = 4.4 μM, C_0(sulfite) = 0.5 mM, C_0(catalyst) = 200 mg L^{-1}, initial pH = 7.2, V = 20 mL, temperature = 293 K.

concentrations of leached metal ions, such as Zn^{2+}, Cu^{2+}, and Fe^{3+}, from $Zn_{0.8}Cu_{0.2}Fe_2O_4$ were measured during photocatalysis at the optimum operation parameters as well (i.e., initial pH = 7, loading of catalyst = 200 mg L^{-1}, and initial concentration of sulfite = 0.5 mM). The concentrations of Zn^{2+} and Fe^{3+} were as low as 0.06 and 0.29 mg L^{-1}, respectively, while Cu^{2+} was below the detection limit (0.00824 mg L^{-1}) of the instrument (Table S2 in Supporting Information). The recommended limits for Zn^{2+}, Cu^{2+}, and Fe^{3+} in reclaimed water for irrigation (long-term) are 2.0, 0.2, and 5.0 mg L^{-1}, respectively [31], indicating the safety of the proposed treatment process.

3.3. Influence of operating parameters on the degradation of atrazine

3.3.1. Influence of initial concentration of sulfite and $Zn_{0.8}Cu_{0.2}Fe_2O_4$ loading

The effects of catalyst loading and initial concentration of sulfite on the degradation of atrazine were studied separately (Figs. 5a and b). The observed kinetic rate constant (k_{obs}) increased rapidly with the rise of catalyst loading from 20 to 100 mg L^{-1} before slowing (the rate of change slowed at higher concentrations). In the range of 0–100 mg L^{-1}, the rise in amount of catalyst can provide more surface area and available active sites, resulting in higher degradation of atrazine. However, in the range of 200–400 mg L^{-1}, the excessive catalyst not only limited the diffusion of sulfite and atrazine to the solid surface of catalysts, but also inhibited the penetration of UV–vis light, which lowered the efficiency of luminous energy utilization.

Similarly, the initial sulfite concentration has a positive influence in a relatively low concentration range, but it has a negative influence in the case of overdose. Although more sulfite could generate more active oxidant species, it would compete with the target contaminant for the oxidant species (Eq. (6)) [1]. Thus, the following experiments were conducted with 200 mg L^{-1} catalyst and 0.5 mM sulfite based on the results of the effect of catalyst loading and sulfite dosing on the degradation of atrazine.

$$SO_4^{\bullet-} + HSO_3^- \rightarrow H^+ + SO_4^{2-} + SO_3^{\bullet-} \quad (6)$$

3.3.2. Influence of surface hydroxyl groups

The influence of the surface hydroxyl groups (–OH) was investigated by competitive experiments through adding phosphate ions, which have a high affinity for –OH [30,32] (Fig. 5c). The apparent reaction rate constant decreased dramatically from 0.195 to 0.013 min^{-1} when 1 mM phosphate ions were present (initial pH = 7). Additionally, with the increase in the concentration of phosphate ions from 1 to 10 mM, the degradation efficiency of atrazine continuously

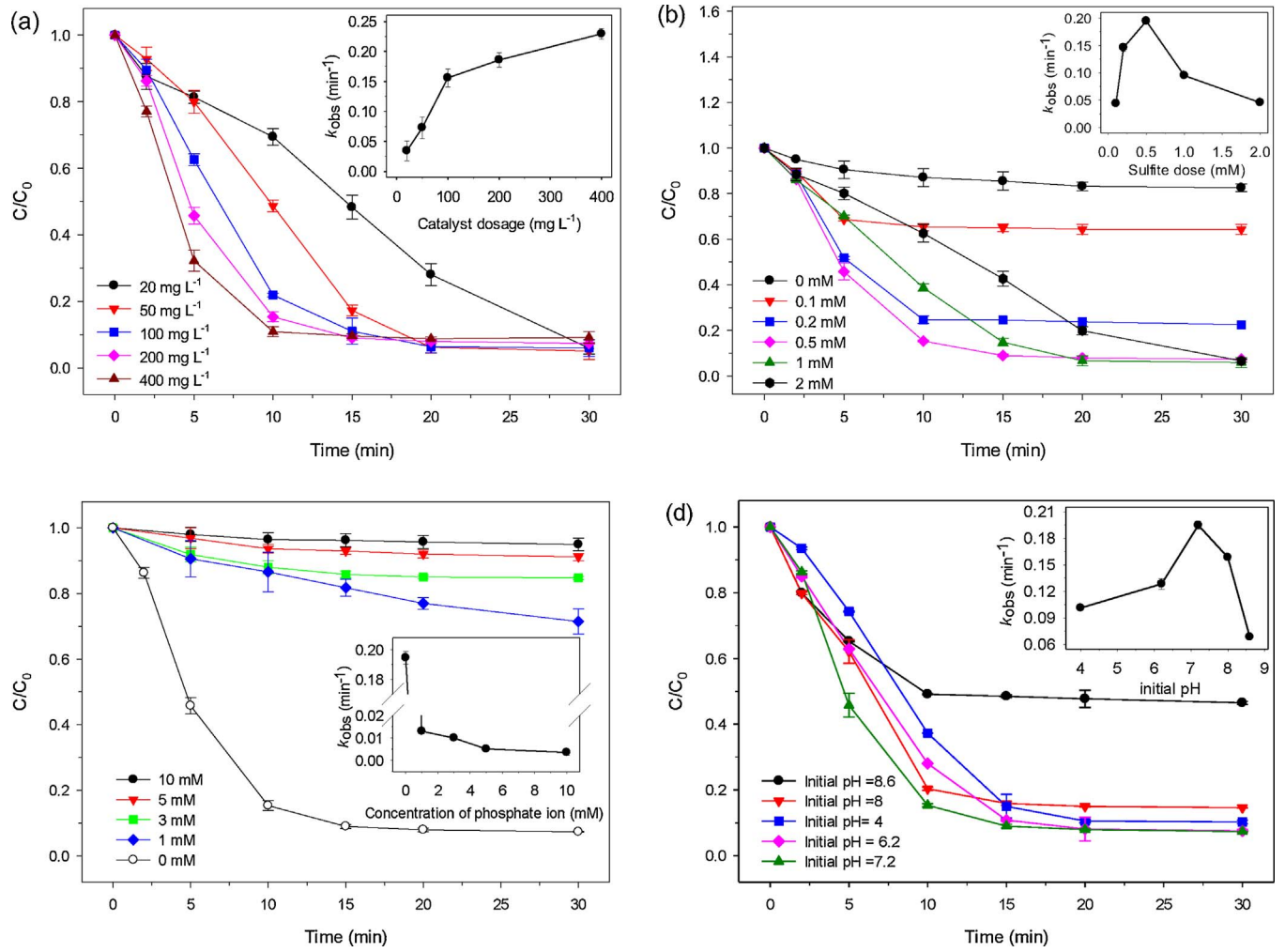

Fig. 5. Effect of catalyst loading (a), sulfite dosages (b), phosphate ion (c), and initial pH (d) on atrazine degradation in UV–vis light/$Zn_{0.8}Cu_{0.2}Fe_2O_4$/sulfite. General conditions: C_0(atrazine) = 4.4 μM, C_0(sulfite) = 0.5 mM, C_0(catalyst) = 200 mg L^{-1}, initial pH = 7.2, V = 20 mL, temperature = 293 K.

declined in the UV–vis light/$Zn_{0.8}Cu_{0.2}Fe_2O_4$/sulfite system. Although the phosphate ions can quench sulfate radicals ($k_{SO_4^{\bullet-}/H_2PO_4} < 7 \times 10^4$ L $mol^{-1}s^{-1}$, pH = 7 [33]), the inhibition phenomenon caused by 1 mM phosphate was much stronger than that caused by 50 mM t-BuOH ($k_{SO_4^{\bullet-}/t\text{-BuOH}} \approx 7 \times 10^4$ L $mol^{-1}s^{-1}$ [33]), indicating that the quenching effect of phosphate ions was not the primary reason. Instead, the main reason might be the replacement of –OH groups on the surface of the catalyst by phosphate ions, leading to less adsorbed oxygen and sulfite [13], fewer reactive species, and thus a lower kinetic reaction rate [25]. Therefore, –OH groups on the surface of the catalyst play a crucial role in the photocatalysis of sulfite by $Zn_{0.8}Cu_{0.2}Fe_2O_4$.

3.3.3. *Influence of the initial pH values*

The initial pH of reaction solutions is an important parameter for the decomposition of atrazine because of its influence on the active sites of ferrite and the formation of metal-sulfito complexes. Initial pH values of 4.0, 6.2, 7.2, 8.0 and 8.5 were selected in the UV–vis light/$Zn_{0.8}Cu_{0.2}Fe_2O_4$/sulfite system. Since the sulfite was oxidized along with the destruction of atrazine (Fig. S4 in Supporting Information), the pH of the reaction solution decreased gradually to almost 3.5 in 30 min (Fig. S5 in Supporting Information). As shown in Fig. 5d, the apparent rate constant rose with increasing pH in the acidic region (4–7), but decreased dramatically in the basic pH region (7–8.5).

Firstly, the surface charge of ferrite depends on the pH due to the protonation and deprotonation of surface –OH groups. The surface –OH groups were characterized by the zeta potential at varied pH values (Fig. S6 in Supporting Information). $Zn_{0.8}Cu_{0.2}Fe_2O_4$ had a point of zero charge (pH_{pzc}) at a pH of around 8.1, indicating that the surface charge is positive at pH < 8.1 and negative when pH > 8.1. In addition, atrazine and sulfite were presented as negative ions at selected pH values. Since electrical attraction is ideal compared to electrical repulsion for the heterogeneous reaction [34], a pH below 8.1 is preferred for the photocatalytic activity of sulfite by $Zn_{0.8}Cu_{0.2}Fe_2O_4$ to degrade atrazine.

Moreover, the solution pH can affect the formation rate of metal-sulfito complexes that can subsequently decompose to generate sulfite radical. In the pH range of 3–8, O-bonded metal-sulfito complexes were formed. However, when the pH was higher than 9, S-bonded metal-sulfito complexes were generated at a lower rate [13]. Hence, the slow formation of S-bonded metal-sulfito complexes was probably one of the reasons for the drastic decline in the degradation of atrazine at a high pH.

Additionally, an acidic condition (pH = 4.0) was reported as an optimum condition for the Fe(III)-S(IV) related homogeneous catalytic process [1,17]. The high efficiency of the photocatalytic activation of sulfite by $Zn_{0.8}Cu_{0.2}Fe_2O_4$ at a neutral pH highlights its advantage, and therefore it has promise as a feasible technology for wastewater treatment.

3.4. Reactive species and possible mechanisms

3.4.1. Identification of primary reactive species

The activation of sulfite by ferrite under UV–vis light might produce several main radicals, namely hydroxyl, sulfite, sulfate, and peroxy-sulfate radicals. The ·OH might be generated by a series of reactions between adsorbed oxygen and photo-generated electrons (e^-) on the surface of $Zn_{0.8}Cu_{0.2}Fe_2O_4$. The sulfite radical ($SO_3\cdot^-$) was probably generated from the oxidation of sulfite by the photo-generated holes (h^+) and the decomposition of metal-sulfito complexes (Fe(III)-sulfito and Cu(II)-sulfito) that are accelerated by UV–vis light irradiation. The peroxy-sulfate radical ($SO_5\cdot^-$) and $SO_4\cdot^-$ could be transformed from the oxidation of sulfite radical by dissolved O_2 in water. Due to the low oxidation potential of $SO_3\cdot^-$ and $SO_5\cdot^-$ ($E^0(SO_3\cdot^-)$ = 0.63 V [35] and $E^0(SO_5\cdot^-)$ = 0.81 V [33]), they were not considered as dominant reactive oxidants for the degradation of atrazine in the presence of ·OH and $SO_4\cdot^-$.

To identify the predominant oxidant species, several attempts were performed: the photoluminescence technique using TPA, radical quenching experiments, and monitoring two specific byproducts by QQQ-LC/MS. TPA is used as the ·OH dosimeter since it is a non-fluorescent compound and has a high affinity with ·OH rather than with $SO_4\cdot^-$. The reaction between ·OH and TPA leads to the formation of a highly fluorescent compound (TPA-OH) (Fig. 6a). As shown in Fig. 6b, a small amount of ·OH was generated on the surface of the catalysts under UV–vis light, which was significantly prompted by adding sulfite, indicating the presence of ·OH in the UV–vis light/$Zn_{0.8}Cu_{0.2}Fe_2O_4$/sulfite system. Additionally, the signal of TPA-OH in UV–vis light/sulfite was non-negligibly high, because TPA can react rapidly with hydrated electrons (e^-_{aq}) that are produced by the UV-activated SO_3^{2-} (Eq. (7)) [36,37].

$$SO_3^{2-} + h\nu \rightarrow SO_3^{\bullet -} + e^-_{aq} \quad (7)$$

For revealing the existence of $SO_4\cdot^-$, ethanol (EtOH) and ter-butyl alcohol (t-BuOH) with different initial concentrations were used as scavengers in the UV–vis light/$Zn_{0.8}Cu_{0.2}Fe_2O_4$/sulfite system. Alcohols with α-hydrogen, such as EtOH, can react rapidly with both ·OH and $SO_4\cdot^-$, while alcohols without α-hydrogen such as t-BuOH can only react fast with ·OH. The kinetic rate constants between these two radicals and several chemicals (including atrazine, EtOH and t-BuOH) are shown in Table S3 in Supporting Information [32,38]. As shown in Fig. 7, EtOH at all selected concentrations (5–30 mM) could remarkably inhibit the degradation of atrazine. In the case of t-BuOH, the degradation efficiency of atrazine in this system decreased with the increase in the concentration of t-BuOH (10–100 mM). It was assumed

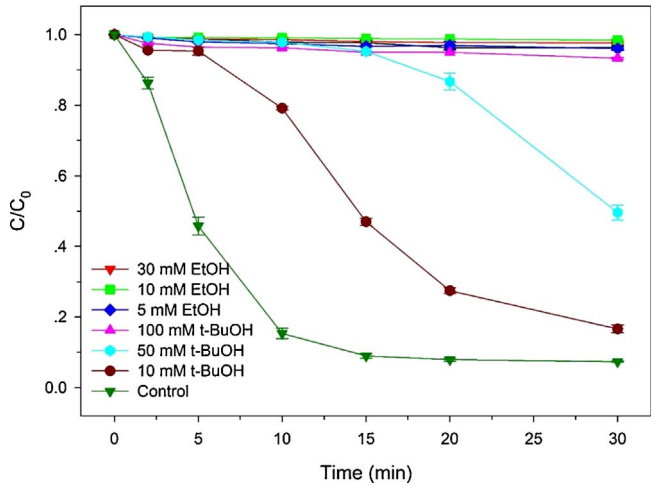

Fig. 7. Effect of radicals scavengers on atrazine degradation in UV–vis light/$Zn_{0.8}Cu_{0.2}Fe_2O_4$/sulfite system. Reaction conditions: C_0(atrazine) = 4.64 μM, C_0(sulfite) = 0.5 mM, C_0(catalyst) = 200 mg L^{-1}, initial pH = 7.2, V = 20 mL, temperature = 293 K.

that 10 mM of t-BuOH could compete with 4.64 μM of atrazine for most of ·OH because $C_{t\text{-BuOH}} \times k_{OH/t\text{-BuOH}}$ was 2 orders of magnitude larger than $C_{atrazine} \times k_{\cdot OH/atrazine}$. Therefore, it is possible to attribute the difference between the removal efficiency of atrazine in the presence of EtOH and t-BuOH at low concentration to the formation of $SO_4\cdot^-$.

However, the difference of the degradation efficiency of atrazine in the presence of EtOH or t-BuOH might result from their different affinity to the surface of catalysts [14]. Atrazine-desethyl (DEA) and atrazine-desisopropyl (DIA) were thus quantified by QQQ-LC/MS to further explore the roles of ·OH and $SO_4\cdot^-$ in the destruction of atrazine by UV–vis light/$Zn_{0.8}Cu_{0.2}Fe_2O_4$/sulfite (Fig. 8). DEA and DIA can be formed by both ·OH and $SO_4\cdot^-$ and their concentrations are linear to the concentration of atrazine (Eqs. 8–9), but k_1/k_2 is quite different for these two formation pathways. In the case of ·OH-induced degradation of atrazine, the k_1/k_2 is near 3 [32] because ·OH is a non-selective oxidant, resulting in less of a difference in the concentration of DEA and DIA. However, the k_1/k_2 is about 10 with $SO_4\cdot^-$ as the main reactive species since $SO_4\cdot^-$ prefers to attack conjugated bonds [39], which leads to the prevalence of DEA [32]. At the optimum reaction conditions (i.e., initial pH = 7, loading of catalyst = 200 mg L^{-1}, and initial concentration of sulfite = 0.5 mM), the k_1 is 1.8493 with an intercept of −0.1520, and the standard errors of the slope and the

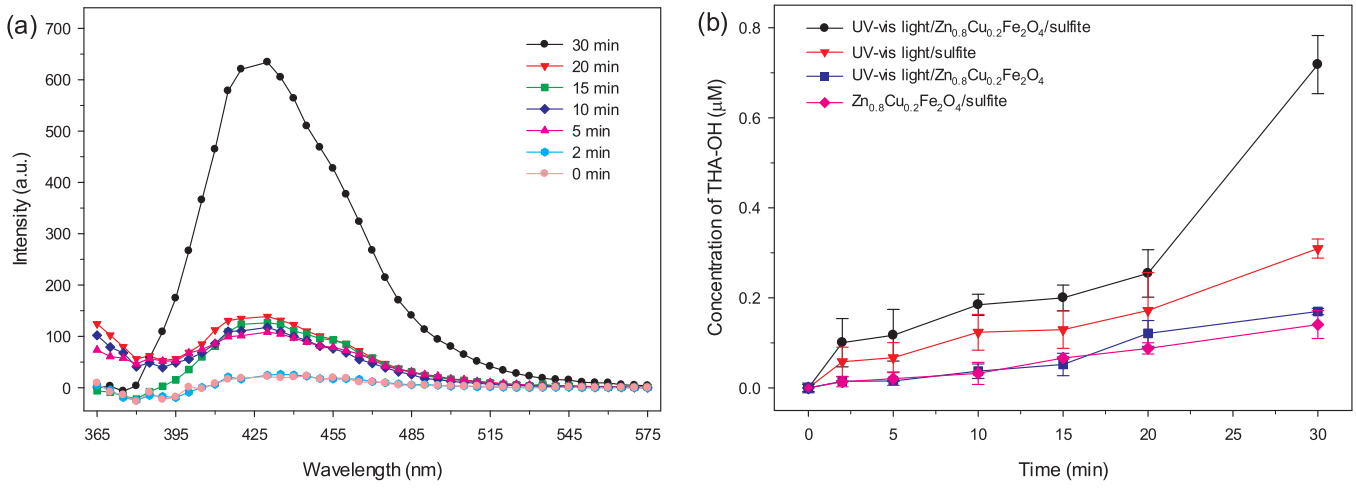

Fig. 6. Fluorescence spectrum of 2-hydroxyl terephthalic acid (TPA-OH) in UV–vis light/$Zn_{0.8}Cu_{0.2}Fe_2O_4$/sulfite (a); concentration of 2-hydroxyl terephthalic acid (TPA-OH) in different conditions (b). Reaction conditions: C_0(TPA) = 200 μM, C_0(sulfite) = 0.5 mM, C_0(catalyst) = 200 mg L^{-1}, initial pH = 7.2, V = 20 mL, temperature = 293 K.

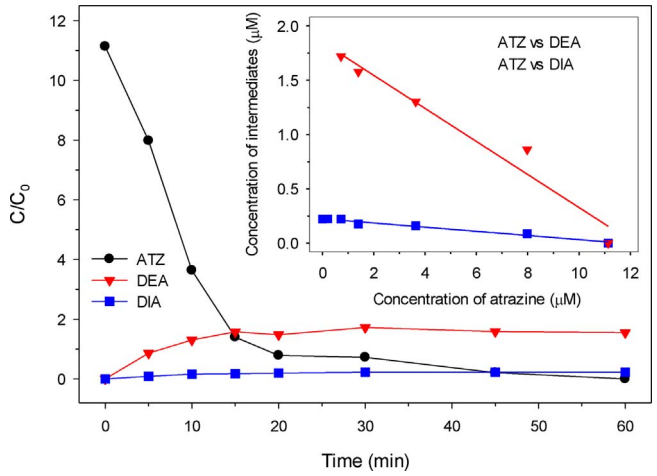

Fig. 8. Atrazine, DEA and DIA removal in UV–vis light/$Zn_{0.8}Cu_{0.2}Fe_2O_4$/sulfite system and (insert) linear regression of atrazine degradation versus DEA and DIA formation. Reaction conditions: C_0(atrazine) = 11.14 μM, C_0(sulfite) = 0.5 mM, C_0(catalyst) = 200 mg L^{-1}, initial pH = 7.2, V = 20 mL, temperature = 293 K.

insert are 0.1163 and 0.0182, respectively (Fig. 8 insert). The k_2 is 0.2248 with an intercept of −0.0193, and the standard errors of the slope and the insert are 0.0127 and 0.0020, respectively (Fig. 8 insert). Therefore, the k_1/k_2 was about 8 in the current reaction, demonstrating that ·OH and $SO_4\cdot^-$ both existed, but $SO_4\cdot^-$ played a more significant role in the degradation of atrazine.

$$\frac{d[DEA]}{dt} = -k_1 \times \frac{d[ATZ]}{dt} \rightarrow \frac{d[DEA]}{d[ATZ]} = -k_1 \quad (8)$$

$$\frac{d[DIA]}{dt} = -k_2 \times \frac{d[ATZ]}{dt} \rightarrow \frac{d[DIA]}{d[ATZ]} = -k_2 \quad (9)$$

3.4.2. Identification of active sites

The photo-heterogeneous activation of sulfite by ferrite and its active sites have not been reported previously. To find out the primary functional sites, the surface valence states of fresh and used $Zn_{0.8}Cu_{0.2}Fe_2O_4$ were investigated through XPS analysis. In accordance with the NIST XPS database, the peak at 1021.4 eV was assigned to Zn $2p_{3/2}$, indicating the presence of ≡Zn(II) (Fig. 9a). In O 1s spectra (Fig. 9b), peaks at 530 eV and 532 eV were assigned to lattice oxygen, and surface hydroxyl groups and adsorbed oxygen, respectively [40]. In Fig. 9c, the peaks centered at 933.8 eV with a satellite peak at 936.5–944 eV corresponded to Cu $2p_{3/2}$. The Cu 2p spectrum was composed of two sets of peaks at 933 and 934 eV, which could be assigned to the chemical states of ≡Cu(I) and ≡Cu(II), respectively [40]. The two distinct peaks centered at 710.8 and 724.6 eV with a shake-up satellite at 716.3-721.3 eV in Fig. 9d could be ascribed to the binding energy of Fe $2p_{3/2}$ and Fe $2p_{1/2}$, respectively. The spectrum of Fe $2p_{3/2}$ could be fitted into four contributions, where the peak at 709.8 eV was assigned to ≡Fe(II) and the other three referred to ≡Fe(III) [41]. The slight shift of the Cu $2p_{3/2}$ and Fe $2p_{3/2}$ peaks suggests that the ratio of ≡Cu(I)/≡Cu(II) and ≡Fe(II)/≡Fe(III) changed after the photocatalytic reaction [42]. The Cu $2p_{3/2}$ and Fe $2p_{3/2}$ peaks increased by 15% and 4%, respectively, indicating that part of ≡Cu(II) and ≡Fe(III) on the surface of $Zn_{0.8}Cu_{0.2}Fe_2O_4$ was transformed to a reductive valence state. In addition, ≡Fe(III) is thermodynamically likely to be reduced by ≡Cu(I), as shown in Eq. (10) [41], leading to more ≡Cu(II) and ≡Fe(II); however, the rate of sulfite oxidation by ≡Fe(III) is the highest among ≡Cu(I), ≡Cu(II), ≡Fe(II), and ≡Fe(III) [13]. This accounts for the weaker photocatalytic ability of $Zn_{0.8}Cu_{0.2}Fe_2O_4$ compared to $ZnFe_2O_4$.

$$\equiv Cu^{I} + \equiv Fe^{III} \rightarrow \equiv Cu^{II} + \equiv Fe^{II} \quad (10)$$

3.4.3. Possible photocatalysis mechanisms of sulfite

Based on the discussion above, a probable photocatalytic mechanism of sulfite by $Zn_{0.8}Cu_{0.2}Fe_2O_4$ under UV–vis light irradiation could be deduced, as shown in Fig. 10. Under the irradiation of UV–vis light, $Zn_{0.8}Cu_{0.2}Fe_2O_4$ was activated to generate e^--h^+ pairs (Eq. (11)) [18,19]. The formed e^- could react with adsorbed O_2 to generate a superoxide radical ($^{\bullet}O^-_{2(ads)}$), which could be transformed to a hydroperoxyl radical ($HO_2\cdot$) and ·OH (Eqs. (12)–(15)) [18,19,43]. Furthermore, we proposed the formed h^+ might be reduced by HSO_3^-/SO_3^{2-} adsorbed on the surface of the catalyst to form $SO_3\cdot^-$ (Eqs. (16)–(17)), because h^+ has a high oxidation potential that can react with many salts (i.e., SO_4^{2-}) to generate the corresponding radicals (i.e., $SO_4\cdot^-$) [44]. In addition, the light irradiation probably accelerated the decomposition of metal-sulfito complexes, such as Fe(III)-sulfito and Cu(II)-sulfito, to produce $SO_3\cdot^-$ (Eqs. (18) – (21)) [1,16]. Although the oxidation potential of $SO_3\cdot^-$ is low, it could quickly react with dissolved O_2 to form $SO_5\cdot^-$ ($k = (1.1 - 2.5) \times 10^9$ L $mol^{-1}s^{-1}$ [45]) and subsequently $SO_4\cdot^-$ (Eqs. (2)–(5)) [1,13]. Finally, the atrazine was degraded by the generated ·OH and $SO_4^{\cdot -}$.

$$Zn_{0.8}Cu_{0.2}Fe_2O_4 + h\nu \rightarrow Zn_{0.8}Cu_{0.2}Fe_2O_4(h^+ + e^-) \quad (11)$$

$$Zn_{0.8}Cu_{0.2}Fe_2O_4\ (e^-) + O_{2(ads)} \rightarrow Zn_{0.8}Cu_{0.2}Fe_2O_4 + {}^{\bullet}O^-_{2(ads)} \quad (12)$$

$${}^{\bullet}O^-_{2(ads)} + H^+ \rightarrow HO_2{}^{\bullet} \quad (13)$$

$$2HO_2{}^{\bullet} \rightarrow O_2 + H_2O_2 \quad (14)$$

$$H_2O_2 + {}^{\bullet}O^-_{2(ads)} \rightarrow OH^- + {}^{\bullet}O\ H + O_2 \quad (15)$$

$$Zn_{0.8}Cu_{0.2}Fe_2O_4(h^+) + HSO_3^- \rightarrow Zn_{0.8}Cu_{0.2}Fe_2O_4 + SO_3{}^{\bullet -} + H^+ \quad (16)$$

$$Zn_{0.8}Cu_{0.2}Fe_2O_4(h^+) + SO_3^- \rightarrow Zn_{0.8}Cu_{0.2}Fe_2O_4 + SO_3{}^{\bullet -} \quad (17)$$

$$\equiv Fe(III)\text{-}OH + HSO_3^- \rightarrow \equiv Fe(III)\text{-}O\text{-}SO_2^- + H_2O \quad (18)$$

$$\equiv Fe(III)\text{-}O\text{-}SO_2^- + h\nu \rightarrow \equiv Fe(II) + SO_3{}^{\bullet -} \quad (19)$$

$$\equiv Cu(II)\text{-}OH + HSO_3^- \rightarrow \equiv Cu(II)\text{-}O\text{-}SO_2^- + H_2O \quad (20)$$

$$\equiv Cu(II)\text{-}O\text{-}SO_2^- + h\nu \rightarrow \equiv Cu(I) + SO_3{}^{\bullet -} \quad (21)$$

3.5. Transformation products and potential degradation mechanisms

3.5.1. Identification of transformation products

The transformation products of atrazine in the UV–vis light/$Zn_{0.8}Cu_{0.2}Fe_2O_4$/sulfite system were detected by Q-TOF-LC/MS. Their molecular structures were proposed based on the measured mass-to-charge ratio (*m/z*) and comparison with literature spectra. In the present study, up to 16 byproducts were detected. Their *m/z*, molecular formula, name, abbreviation previously used [46], and structure are shown in Table S4 in Supporting Information. Due to the complicated radical reaction mechanisms, isomers might exist for several *m/z* values. Therefore, Spartan 14 was used to calculate the relative energies of isomers to consider the one with the lowest energy for a certain *m/z* value. The calculated results are shown in Table S5 in Supporting Information. According to their chemical structure, these byproducts were classified into three groups: i) chlorinated derivatives (Fig. 11a), ii) dechlorinated-hydroxylated derivatives (Fig. 11b), and iii) dechlorinated-hydrogenated derivatives (Fig. 11c).

3.5.2. Possible degradation mechanisms of atrazine

3.5.2.1. Oxidation on the lateral chains. Most detected byproducts were formed due to the oxidation processes of atrazine on the later chains: dealkylation (Fig. S7b in Supporting Information), alkylic-hydroxylation, olefination, and alkylic-oxidation (Scheme S7c in Supporting Information). The initial step of these oxidation processes was the formation of C (C4 or C5)-centered radicals (Fig. S7a in Supporting Information) [32]. On the one hand, C-centered radicals

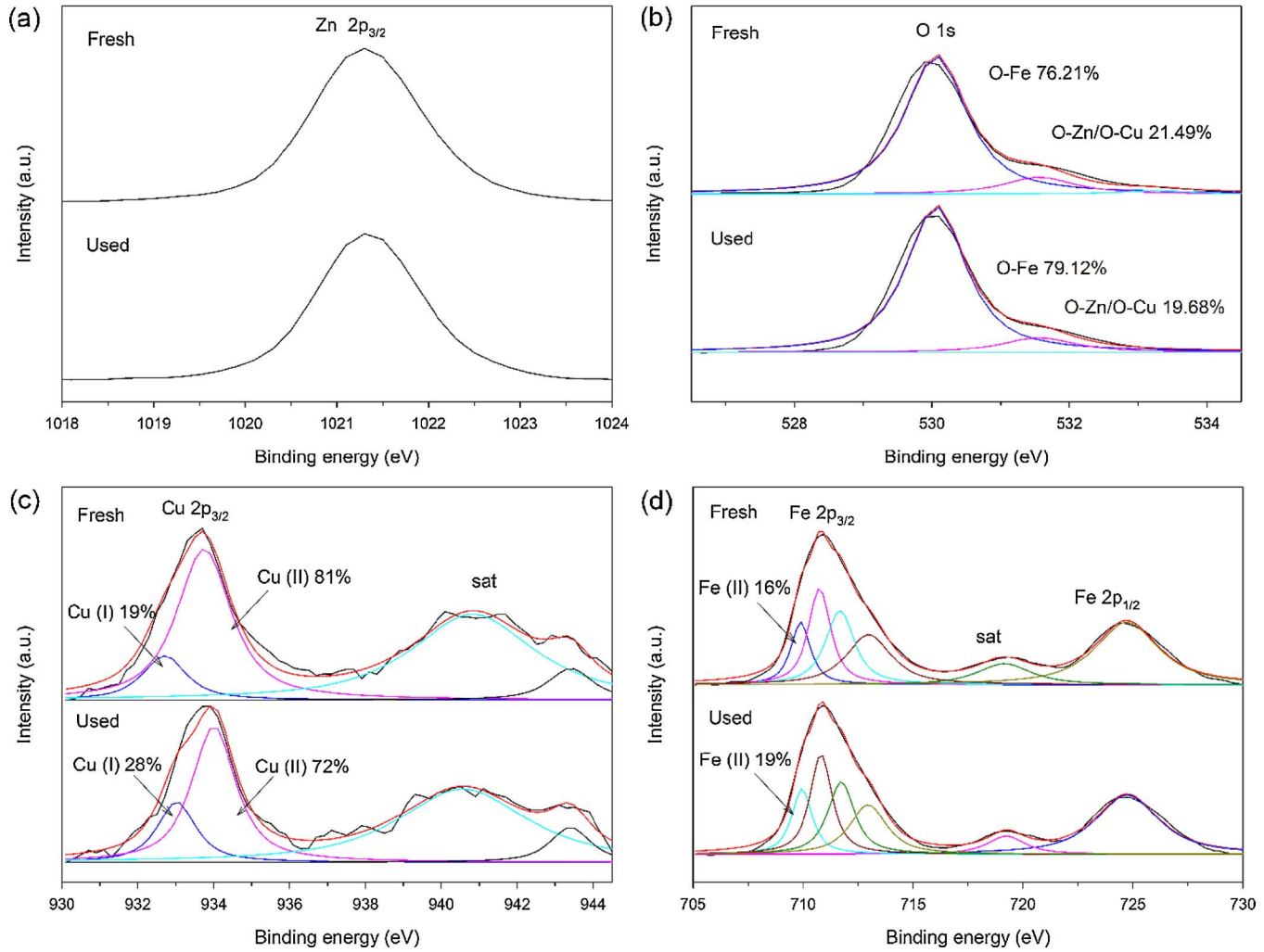

Fig. 9. XPS survey on Zn 2p (a), O 1s (b), Cu 2p (c), and Fe 2p (d) of fresh and used catalysts.

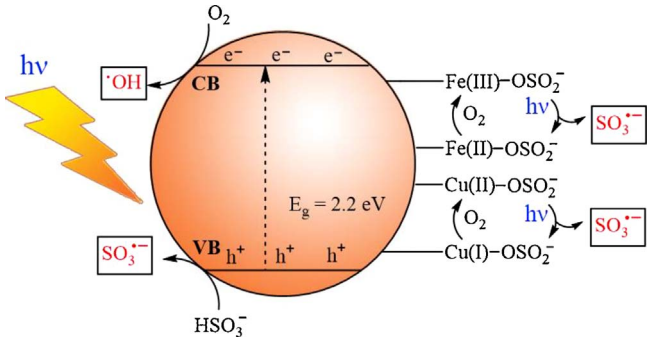

Fig. 10. Possible photocatalytic mechanisms.

might be transformed by a 1,2-H shift from N (exocyclic)-centered radicals that are formed through electron transfer in a $SO_4\cdot^-$-based oxidation process [32]; on the other hand, C-centered radicals could be generated through α-H abstraction by $SO_4\cdot^-$ [47]. Compared to the C5-centered radical, the C4-centered radical has a lower energy (Table S5 in Supporting Information), leading to the prevalence of byproducts with the N-isopropyl group (Fig. 12).

As shown in Scheme S2 in Supporting Information, the C-centered radical could be attacked by dissolved O_2 to form a peroxide radical, which subsequently produced per-hydroxyl radical ($HO_2\cdot$) and olefination byproducts, such as CVIT (*m/z* 214.085), CVAT (*m/z* 172.038), and OVIT (*m/z* 196.119) [46,48]. It is interesting that the double bond is in the form of N = C − C when −Cl attaches to C1, while in the form of N − C = C when −OH attaches to C1 based on the calculated energy, which might be caused by the weaker inductive effect of −OH than that of −Cl. Further oxidation of olefination byproduct led to the formation of acetaldehyde and the dealkylated products, such as DEA (*m/z* 188.069), DIA (*m/z* 174.054), and OAIT (*m/z* 170.103) [46,49].

In addition, continuous attacking on the C-centered radical by ·OH led to the generation of alkylic-hydroxylation byproducts, CNIT (*m/z* 232.095) and ONIT (*m/z* 214.180), which could be further oxidized to form imine and aldehyde transformation products [46,49,50]. Imine byproducts were transformed via the dehydration of alkylic-hydroxylation byproducts [46,49]. Additionally, as shown in Fig. S7c in Supporting Information, the H-abstraction by $SO_4\cdot^-$ on −OH bonded C could lead to the formation of aldehyde byproducts [49], namely CDIT (*m/z* 230.080) and ODIT (*m/z* 212.114), which were detected at high concentrations.

3.5.2.2. Dechlorination-hydroxylation. A certain amount of the transformation products of atrazine underwent the dechlorination-hydroxylation pathway by replacing Cl atoms with OH groups in three steps, as shown in Fig. S7d in Supporting Information [50,51]. In the initial stage, atrazine reacted with $SO_4\cdot^-$ via electron transfer to produce a radical cation ($[C_8H_{14}ClN_5]\cdot$) [50]. C1 of the radical cation was the preferable site for the nucleophilic reaction of water molecules due to the induction effect of the chlorine atom, leading to the forming of an OH-adduct [52]. Following a heterolytic cleavage of C − Cl bond

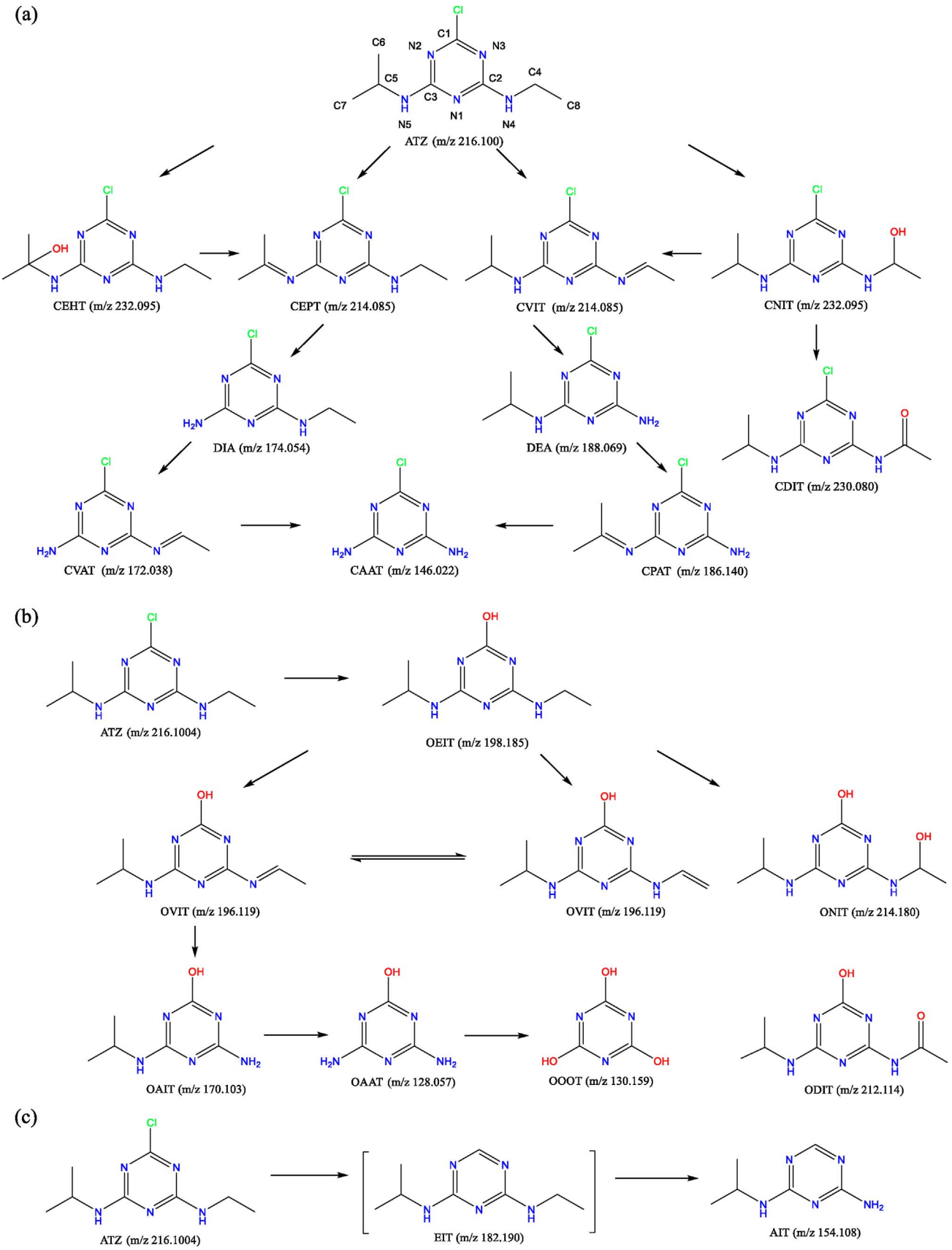

Fig. 11. Probable degradation pathways of atrazine.

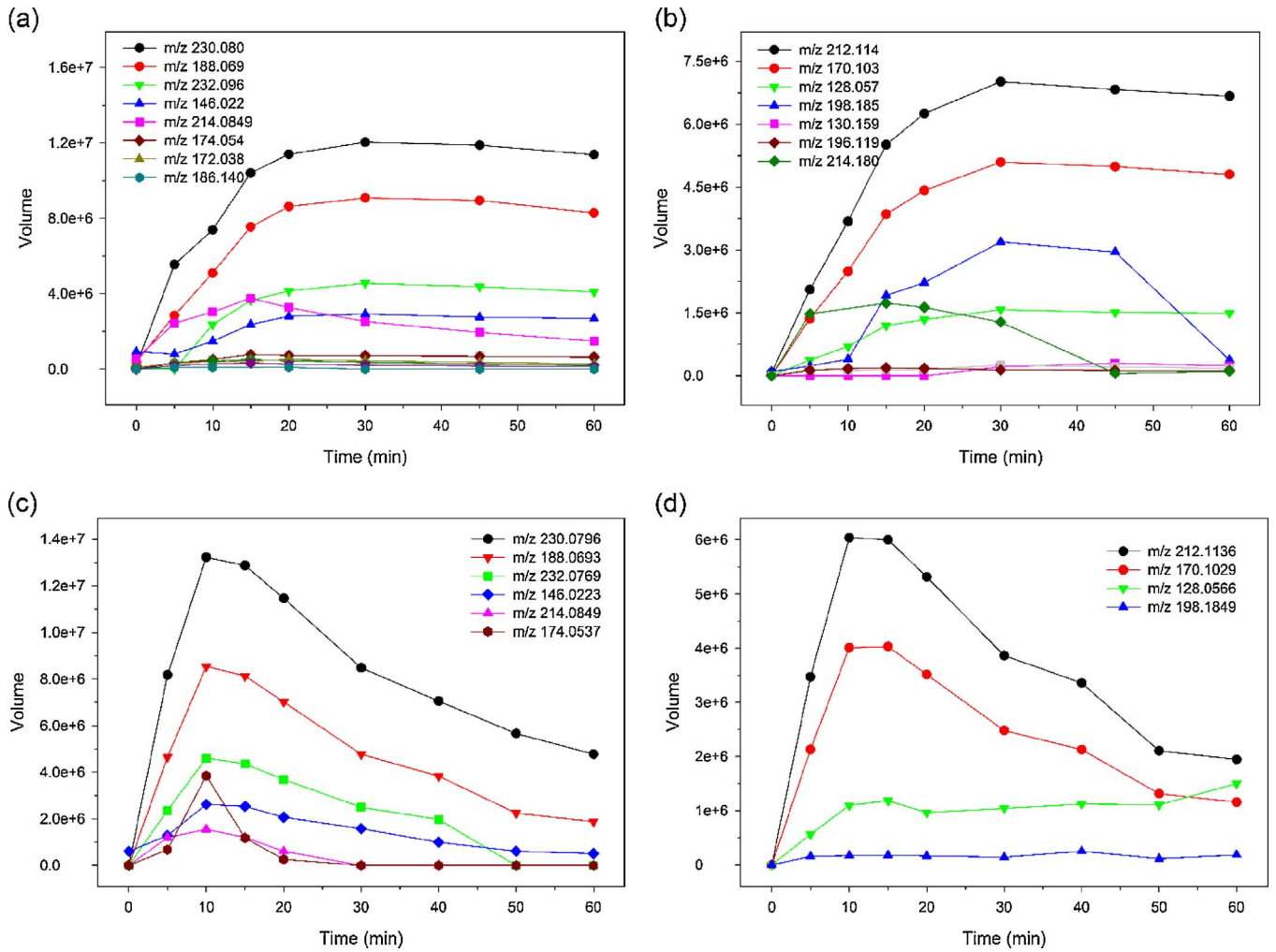

Fig. 12. Evolution of byproducts of atrazine in the UV–vis light/$Zn_{0.8}Cu_{0.2}Fe_2O_4$/sulfite system with one addition of 1 mM sulfite (a) and multiple addition of 0.8 mM sulfite (0.2 mM at each time). Reaction conditions: C_0(atrazine) = 9.28 μM, C_0(catalyst) = 200 mg L^{-1}, initial pH = 7.2, V = 20 mL, temperature = 293 K.

of the OH-adduct, dechlorinated-hydroxylated derivatives were generated [46].

3.5.2.3. Dechlorination-hydrogenation. The dechlorination-hydrogenation intermediate (EIT) was not detected in this process; nevertheless, its subsequent de-alkylation byproduct (AIT, *m/z* 154.108) was detected along with the degradation of atrazine. There were three possible reasons accounting for the dechlorination-hydrogenation pathway. Firstly, the short-wavelength irradiation in UV–vis light mightcause the cleavage of the C − Cl bond of atrazine, because EIT was also detected during the UV-C photolysis [46], and the amount of produced hydroquinone from 2,4-dichlorophenol was much larger in the UV-C/H_2O_2 process than in the Fenton process [53]. Secondly, as mentioned before, atrazine could be directly reduced by sulfite, although its rate was slow [30]. Moreover, the existence of ≡Fe(II) on the surface of the catalyst could have followed the pathway for dechlorinating atrazine through Eq. (20) [54].

$$2 \equiv Fe(II) + RX + H^+ \rightarrow 2 \equiv Fe(III) + RH + X^- \quad (20)$$

All the different pathways mentioned above might process simultaneously and crosslink to each other to form various transformation products. Furthermore, the toxicity of the transformation products of atrazine is related to the Cl atom [55], which suggests that the dechlorinated derivatives are less toxic among the produced byproducts in wastewater treatment process.

3.6. Sulfite addition in multiple low-concentration aliquots

According to Figs. 12a and b, the removal efficiency of the transformation products of atrazine was low in the UV–vis light/$Zn_{0.8}Cu_{0.2}Fe_2O_4$/sulfite system, especially for the chlorinated byproducts. Therefore, adding sulfite in multiple low-concentration aliquots was used to improve the destruction efficiency of byproducts of atrazine, possibly reduce the toxicity. In the case of one addition of 1 mM sulfite, most transformation products reached their maximum concentration at 30 min and could not be further decomposed after 30 min by the UV–vis light/$Zn_{0.8}Cu_{0.2}Fe_2O_4$/sulfite method, except for the intermediates with *m/z* of 214.085, 198.185, and 154.108. However, when 0.8 mM of sulfite was added in four consecutive times equally, some transformation products such as *m/z* of 172.038, 232.096, 130.159, 198.148, 196.119, 214.180, and 154.108 were no longer detected (Figs. 12c and d). The present transformation products reached their maximum concentration at 10 min and could be further destroyed after 10 min. The inefficient removal of atrazine transformation products in the case of one addition of 1 mM of sulfite may result from a competitive reaction between sulfite and reactive oxidants (·OH, $SO_4^{\cdot -}$, etc.) [40]. These results indicate that UV–vis light/$Zn_{0.8}Cu_{0.2}Fe_2O_4$/sulfite with multiple low-concentration aliquots of sulfite addition is promising to efficiently remove not only the target contaminant, atrazine, but also other possible toxic transformation products.

4. Conclusion

In summary, magnetic $Zn_xCu_{1-x}Fe_2O_4$ materials were successfully prepared by the sol-gel combustion method, among which $Zn_{0.8}Cu_{0.2}Fe_2O_4$ exhibited the highest photocatalytic ability in the activation of sulfite to degrade atrazine under UV–vis light irradiation. $Zn_{0.8}Cu_{0.2}Fe_2O_4$ retained high photocatalytic activity after four successive cycles, which demonstrated good stability during the reaction. Moreover, $SO_4\cdot^-$ was identified as the main reactive oxidant in this system; it was most likely generated through the oxidation of sulfite by the photo-generated holes and metal atoms (≡Fe(III) and Cu(II)) on the surface of the synthesized catalyst. Additionally, up to 16 transformation products in the degradation of atrazine were detected, but the removal of them was not efficient. Thus, the multiple low-dose addition of sulfite was adopted to improve the degradation efficiency of these byproducts, especially for chlorinated ones, enhancing the destruction and reducing the possible toxicity of atrazine in this proposed treatment method. As in the case of the magnetic removal of used catalysts, sulfite could be completely oxidized along with the decomposition of atrazine, indicating the UV–vis light/$Zn_{0.8}Cu_{0.2}Fe_2O_4$/sulfite system can be a "green" advanced oxidation technology to produce $SO_4\cdot^-$ and remove organic chemicals in wastewater treatment applications.

Acknowledgements

The authors acknowledge financial support from the United States National Science Foundation (grant number CBET-1439314) for this research. Ying Huang acknowledges support from the China Scholarship Council (CSC) scholarship (201306270057). Libor Machala thanks the financial support provided by the project LO1305 of the Ministry of Education, Youth and Sports of the Czech Republic. The authors thank Martin Petr and Ondrej Malina (Palacký University, Olomouc) for characterization of the ferrites by XPS and VSM, respectively.

Appendix A. Supplementary data

Supplementary data associated with this article can be found, in the online version, at http://dx.doi.org/10.1016/j.apcatb.2017.09.001.

References

[1] Y.G. Guo, X.Y. Lou, C.L. Fang, D.X. Xiao, Z.H. Wang, J.S. Liu, Novel photo-Sulfite system: toward simultaneous transformations of inorganic and organic pollutants, Environ. Sci. Technol. 47 (2013) 11174–11181.
[2] Z.Z. Liu, S.J. Yang, Y.N. Yuan, J. Xu, Y.F. Zhu, J.J. Li, F. Wu, A novel heterogeneous system for sulfate radical generation through sulfite activation on a CoFe2O4 nanocatalyst surface, J. Hazard. Mater. 324 (2017) 583–592.
[3] X.X. He, A.A. de la Cruz, D.D. Dionysiou, Destruction of cyanobacterial toxin cylindrospermopsin by hydroxyl radicals and sulfate radicals using UV-254 nm activation of hydrogen peroxide, persulfate and peroxymonosulfate, J. Photochem. Photobiol. a-Chem. 251 (2013) 160–166.
[4] H. Lin, J. Wu, H. Zhang, Degradation of clofibric acid in aqueous solution by an EC/Fe^{3+}/PMS process, Chem. Eng. J. 244 (2014) 514–521.
[5] M.G. Antoniou, A.A. de la Cruz, D.D. Dionysiou, Degradation of microcystin-LR using sulfate radicals generated through photolysis, thermolysis and e(−) transfer mechanisms, Appl. Catal. B-Environ. 96 (2010) 290–298.
[6] X. Duan, X. He, D. Wang, S.P. Mezyk, S.C. Otto, R. Marfil-Vega, M.A. Mills, D.D. Dionysiou, Decomposition of iodinated pharmaceuticals by UV-254 nm-assisted advanced oxidation processes, J. Hazard. Mater. 323 (Part A) (2017) 489–499.
[7] W.S. Chen, Y.C. Su, Removal of dinitrotoluenes in wastewater by sono-activated persulfate, Ultrason. Sonochem. 19 (2012) 921–927.
[8] A. Farhat, J. Keller, S. Tait, J. Radjenovic, Removal of persistent organic contaminants by electrochemically activated sulfate, Environ. Sci. Technol. 49 (2015) 14326–14333.
[9] G.P. Anipsitakis, D.D. Dionysiou, Radical generation by the interaction of transition metals with common oxidants, Environ. Sci. Technol. 38 (2004) 3705–3712.
[10] C. Cai, J. Liu, Z.Y. Zhang, Y.Y. Zheng, H. Zhang, Visible light enhanced heterogeneous photo-degradation of Orange II by zinc ferrite ($ZnFe_2O_4$) catalyst with the assistance of persulfate, Sep. Purif. Technol. 165 (2016) 42–52.
[11] V. Lepentsiotis, R. van Eldik, F.F. Prinsloo, J.J. Pienaar, A kinetic study of the redox behaviour of Fe-III(TPPS) TPPS = 5,10,15,20-tetrakis(p-sulfonato)porphyrinate in the presence of peroxomonosulfate, hydrogen peroxide, and sulfite/oxygen. Direct evidence for multiple redox cycling and suggested mechanisms, J. Chem. Soc.-Dalton Trans. (1999) 2759–2767.
[12] T.N. Das, Reactivity and role of SO_5 center dot- radical in aqueous medium chain oxidation of sulfite to sulfate and atmospheric sulfuric acid generation, J. Phys. Chem. A 105 (2001) 9142–9155.
[13] C. Brandt, R. Vaneldik, Transition-metal-catalyzed oxidation of sulfur(IV) oxides − atmospheric-relevant processes and mechanisms, Chem. Rev. 95 (1995) 119–190.
[14] Y.H. Guan, J. Ma, Y.M. Ren, Y.L. Liu, J.Y. Xiao, L.Q. Lin, C. Zhang, Efficient degradation of atrazine by magnetic porous copper ferrite catalyzed peroxymonosulfate oxidation via the formation of hydroxyl and sulfate radicals, Water Res. 47 (2013) 5431–5438.
[15] Y.G. Zuo, J. Zhan, T.X. Wu, Effects of monochromatic UV-Visible light and sunlight on Fe(III)-catalyzed oxidation of dissolved sulfur dioxide, J. Atmos. Chem. 50 (2005) 195–210.
[16] L. Zhang, L. Chen, M. Xiao, L. Zhang, F. Wu, L.Y. Ge, Enhanced decolorization of orange II solutions by the Fe(II)-Sulfite system under xenon lamp irradiation, Ind. Eng. Chem. Res. 52 (2013) 10089–10094.
[17] L. Chen, X.Z. Peng, J.H. Liu, J.J. Li, F. Wu, Decolorization of orange II in aqueous solution by an Fe(II)/sulfite system: replacement of persulfate, Ind. Eng. Chem. Res. 51 (2012) 13632–13638.
[18] M. Su, C. He, V.K. Sharma, M. Abou Asi, D. Xia, X.-Z. Li, H. Deng, Y. Xiong, Mesoporous zinc ferrite: synthesis, characterization, and photocatalytic activity with H_2O_2/visible light, J. Hazard. Mater. 211 (2012) 95–103.
[19] C. Cai, Z.Y. Zhang, J. Liu, N. Shan, H. Zhang, D.D. Dionysiou, Visible light-assisted heterogeneous Fenton with $ZnFe_2O_4$ for the degradation of Orange II in water, Appl. Catal. B-Environ. 182 (2016) 456–468.
[20] K.X. Zhu, J.H. Wang, Y.J. Wang, C.Z. Jin, A.S. Ganeshraja, Visible-light-induced photocatalysis and peroxymonosulfate activation over $ZnFe_2O_4$ fine nanoparticles for degradation of Orange II, Catal. Sci. Technol. 6 (2016) 2296–2304.
[21] C. Liu, Y.H. Ni, L. Zhang, F. Guo, T.T. Wu, Simple solution-combusting synthesis of octahedral $ZnFe_2O_4$ nanocrystals and additive-promoted photocatalytic performance, RSC Adv. 4 (2014) 47402–47408.
[22] A. Singh, S. Singh, B.D. Joshi, A. Shukla, B.C. Yadav, P. Tandon, Synthesis characterization, magnetic properties and gas sensing applications of $Zn_xCu_{1-x}Fe_2O_4$ ($0.0 < = x < = 0.8$) nanocomposites, Mater. Sci. Semicond. Process. 27 (2014) 934–949.
[23] O.F. Zeck, D.W. Carlyle, Electron-transfer between sulfur(IV) and chloroiron(III) and chlorocopper(II) ions in aqueous chloride media − formation of a sulfur-dioxide complex with chlorocopper(I), Inorg. Chem. 13 (1974) 34–38.
[24] F. Zhang, C. Wei, Y. Hu, H. Wu, Zinc ferrite catalysts for ozonation of aqueous organic contaminants: phenol and bio-treated coking wastewater, Sep. Purif. Technol. 156 (2015) 625–635.
[25] Y.M. Ren, L.Q. Lin, J. Ma, J. Yang, J. Feng, Z.J. Fan, Sulfate radicals induced from peroxymonosulfate by magnetic ferrospinel MFe_2O_4 (M = Co, Cu, Mn, and Zn) as heterogeneous catalysts in the water, Appl. Catal. B-Environ. 165 (2015) 572–578.
[26] R.W. Matthews, The radiation-chemistry of the terephthalate dosimeter, Radiat. Res. 83 (1980) 27–41.
[27] M. Gupta, B.S. Randhawa, Mossbauer, magnetic and electric studies on mixed Rb-Zn ferrites prepared by solution combustion method, Mater. Chem. Phys. 130 (2011) 513–518.
[28] A.I. Borhana, P. Samoila, V. Hulea, A.R. Iordan, M.N. Palamaru, Effect of Al^{3+} substituted zinc ferrite on photocatalytic degradation of Orange I azo dye, J. Photochem. Photobiol. a-Chem. 279 (2014) 17–23.
[29] C.J. Miles, Degradation of aldicarb, aldicarb sulfoxide, and aldicarb sulfone in chlorinated water, Environ. Sci. Technol. 25 (1991) 1774–1779.
[30] K.A. Wulfeck-Kleier, M.D. Ybarra, T.F. Speth, M.L. Magnuson, Factors affecting atrazine concentration and quantitative determination in chlorinated water, J. Chromatogr. A 1217 (2010) 676–682.
[31] U.S.E.P. Agency, U.S.E.P. Agency (Ed.), Guidelines for Water Reuse, 2004.
[32] H.V. Lutze, S. Bircher, I. Rapp, N. Kerlin, R. Bakkour, M. Geisler, C. von Sonntag, T.C. Schmidt, Degradation of chlorotriazine pesticides by sulfate radicals and the influence of organic matter, Environ. Sci. Technol. 49 (2015) 1673–1680.
[33] P. Neta, R.E. Huie, A.B. Ross, Rate constants for reactions of inorganic radicals in aqueous-solution, J. Phys. Chem. Ref. Data 17 (1988) 1027–1284.
[34] Z. Wang, Y. Du, Y. Liu, B. Zou, J. Xiao, J. Ma, Degradation of organic pollutants by $NiFe_2O_4$/peroxymonosulfate: efficiency, influential factors and catalytic mechanism, RSC Adv. 6 (2016) 11040–11048.
[35] P. Neta, R.E. Huie, Free-radical chemistry of sulfite, Environ. Health Perspect. 64 (1985) 209–217.
[36] M. Fischer, P. Warneck, Photodecomposition and photooxidation of hydrogen sulfite in aqueous solution, J. Phys. Chem. 100 (1996) 15111–15117.
[37] X. Li, J. Fang, G. Liu, S. Zhang, B. Pan, J. Ma, Kinetics and efficiency of the hydrated electron-induced dehalogenation by the sulfite/UV process, Water Res. 62 (2014) 220–228.
[38] C.J. Liang, H.W. Su, Identification of sulfate and hydroxyl radicals in thermally activated persulfate, Ind. Eng. Chem. Res. 48 (2009) 5558–5562.
[39] G.P. Anipsitakis, D.D. Dionysiou, Degradation of organic contaminants in water with sulfate radicals generated by the conjunction of peroxymonosulfate with cobalt, Environ. Sci. Technol. 37 (2003) 4790–4797.
[40] Y. Zhang, C. Liu, B. Xu, F. Qi, W. Chu, Degradation of benzotriazole by a novel Fenton-like reaction with mesoporous Cu/MnO_2: Combination of adsorption and catalysis oxidation, Appl. Catal. B: Environ. 199 (2016) 447–457.
[41] Y. Ding, L. Zhu, N. Wang, H. Tang, Sulfate radicals induced degradation of tetrabromobisphenol A with nanoscaled magnetic $CuFe_2O_4$ as a heterogeneous catalyst of peroxymonosulfate, Appl. Catal. B: Environ. 129 (2013) 153–162.

[42] J. Li, S.Y. Sun, C.X. Qian, L. He, K.K. Chen, T.Q. Zhang, Z.L. Chen, M.M. Ye, The role of adsorption in photocatalytic degradation of ibuprofen under visible light irradiation by BiOBr microspheres, Chem. Eng. J. 297 (2016) 139–147.
[43] D.B. Lu, Y. Zhang, S.X. Lin, L.T. Wang, C.M. Wang, Synthesis of magnetic $ZnFe_2O_4$/graphene composite and its application in photocatalytic degradation of dyes, J. Alloys Compd. 579 (2013) 336–342.
[44] M. Ziegmann, T. Doll, F.H. Frimmel, Matrix effects on the photocatalytical degradation of dichloroacetic acid and atrazine in water, Acta Hydroch. Hydrob. 34 (2006) 146–154.
[45] D.T.F. Kuo, D.W. Kirk, C.Q. Jia, The chemistry of aqueous S(IV)-Fe-O_2 system: state of the art, J. Sulfur Chem. 27 (2006) 461–530.
[46] J.A. Khan, X. He, N.S. Shah, H.M. Khan, E. Hapeshi, D. Fatta-Kassinos, D.D. Dionysiou, Kinetic and mechanism investigation on the photochemical degradation of atrazine with activated H_2O_2, $S_2O_8^{2-}$ and HSO_5, Chem. Eng. J. 252 (2014) 393–403.
[47] S. Morimoto, T. Ito, S.I. Fujita, S.I. Nishimoto, A pulse radiolysis study on the reactions of hydroxyl radical and sulfate radical anion with guanidine derivatives in aqueous solution, Chem. Phys. Lett. 461 (2008) 300–304.
[48] J. Andersen, M. Pelaez, L. Guay, Z.H. Zhang, K. O'Shea, D.D. Dionysiou, NF-TiO2 photocatalysis of amitrole and atrazine with addition of oxidants under simulated solar light: emerging synergies, degradation intermediates, and reusable attributes, J. Hazard. Mater. 260 (2013) 569–575.
[49] Y.F. Ji, C.X. Dong, D.Y. Kong, J.H. Lu, Q.S. Zhou, Heat-activated persulfate oxidation of atrazine: implications for remediation of groundwater contaminated by herbicides, Chem. Eng. J. 263 (2015) 45–54.
[50] Y.F. Ji, C.X. Dong, D.A. Kong, J.H. Lu, New insights into atrazine degradation by cobalt catalyzed peroxymonosulfate oxidation: kinetics, reaction products and transformation mechanisms, J. Hazard. Mater. 285 (2015) 491–500.
[51] B. Balci, N. Oturan, R. Cherrier, M.A. Oturan, Degradation of atrazine in aqueous medium by electrocatalytically generated hydroxyl radicals. A kinetic and mechanistic study, Water Res. 43 (2009) 1924–1934.
[52] P. Neta, V. Madhavan, H. Zemel, R.W. Fessenden, Rate constants and mechanism of reaction of sulfate radical anion with aromatic compounds, J. Am. Chem. Soc. 99 (1977) 163–164.
[53] A. Karci, I. Arslan-Alaton, T. Olmez-Hanci, M. Bekbolet, Transformation of 2, 4-dichlorophenol by H_2O_2/UV-C, Fenton and photo-Fenton processes: oxidation products and toxicity evolution, J. Photochem. Photobiol. a-Chem. 230 (2012) 65–73.
[54] B.-Z. Wu, H.-Y. Chen, S.J. Wang, C.M. Wai, W. Liao, K. Chiu, Reductive dechlorination for remediation of polychlorinated biphenyls, Chemosphere 88 (2012) 757–768.
[55] A.B. Baranda, A. Barranco, I.M. de Marañón, Fast atrazine photodegradation in water by pulsed light technology, Water Res. 46 (2012) 669–678.